Landslides (2020) 17:1233–1250
DOI 10.1007/s10346-020-01349-y
Received: 21 October 2019
Accepted: 8 January 2020
Published online: 24 January 2020

Ran Li · Fawu Wang · Shuai Zhang

Controlling role of Ta-d pumice on the coseismic landslides triggered by 2018 Hokkaido Eastern Iburi Earthquake

Abstract The 2018 Hokkaido Eastern Iburi Earthquake triggered massive landslides in the pyroclastic fall deposits. Most of them are shallow debris slides. Based on the field reconnaissance, the shallow debris slides were further categorized into three types: steep translational sliding, gentle translational sliding, and mobilization of V-shaped convergent sliding masses. The three types of shallow landslides were investigated in depth through longitudinal sections, vertical stratigraphic sections, and in situ hardness tests. All three types of shallow landslides were found to initiate from the liquefied failure of the weak Ta-d pumice layer and further evolve to the overall mobilization of the superimposed pyroclastic fall deposits along the liquefied sliding zone. To testify the controlling role and to study the shear behavior as well as the anti-liquefaction strength of the weak Ta-d pumice layer, a series of laboratory tests (basic physical tests and triaxial tests) were conducted on the soils around the sliding zone. The test results indicate that the medium sandy Ta-d pumice MS and the fragile Ta-d pumice CS have lower shear resistance and anti-liquefaction strength than other layers and they can be easily liquefied under intense ground motion. One paleosol layer underlying the Ta-d pumice shows low permeability and enables weathering and soil erosion of the Ta-d pumice, resulting in the widespread existence of the fragile and medium sandy pumice layers in Ta-d. In addition, the positive relationship between coseismic landslide density and Ta-d pumice thickness demonstrates the controlling role of the Ta-d on Iburi landslide occurrence from a macro perspective.

Keywords Iburi earthquake · Ta-d pumice · Shallow debris slide · Triaxial tests · Sliding zone liquefaction

Introduction

At 03:07:59.3 (JST) on 6 September 2018, a Mj 6.7 earthquake (Japan Meteorological Agency 2018a) struck the Eastern Iburi region of Hokkaido, Northern Japan. The epicenter of the main shock is located at 42°41.4′ N, 142°00.4′ E, and the focal depth is approximately 37 km (Geospatial Information Authority of Japan, GSI 2018). The maximum seismic intensity of the Iburi earthquake is 7 on the JMA scale (Japan Meteorological Agency 2018b), and a peak ground acceleration (PGA) of 1.84 g was observed at the HKD127 K-NET station (Fig. 1a) (National Research Institute for Earth Science and Disaster Resilience 2019).

About 5625 landslides (Fig. 1a) were simultaneously triggered by the strong ground motion, and the total affected area was 46.3km^2 (Zhang et al. 2019). The high-mobilized and long runout landslides are responsible for approximately 88% of the casualties (36 out of the 41 deaths) in the Iburi earthquake (Yamagishi and Yamazaki 2018). The widespread occurrence of the landslides and their tremendous destruction attracted extensive attention and concern worldwide. Many studies concerning the spatial distribution and controlling factors of the Iburi landslides have been conducted. In these studies, the controlling effects of the seismic factors, topographic factors, and geological factors were analyzed based on the established landslide inventories (Zhang et al. 2019; Wang et al. 2019; Shao et al. 2019; Zhang and Wang 2019), and the characteristics of the Iburi landslides were described in detail on the basis of field investigations (Hirose et al. 2018; Osanai et al. 2019; Wang 2019). However, the controlling effect of the Ta-d pumice (especially the shear behavior and anti-liquefaction strength of the pumice) on the Iburi landslide occurrence has not been well studied yet.

In this work, the correlation between Iburi landslide distribution and thickness of Ta-d pumice was studied with the aid of ArcGIS, which demonstrates the controlling role of the Ta-d on Iburi landslide occurrence from a macro perspective. Moreover, to investigate the soil composition and the failure mechanism of the Iburi landslides, three concentrated field surveys were conducted in September 2018 and May and June 2019. The investigations cover not only on-site field work but also the visit to a local geological museum and the inquiries of local residents. On the basis of field surveys, the types of shallow debris slides were categorized, the stratigraphic section was classified, and the initiation and the motion features were determined. Then, several laboratory tests, including conventional laboratory tests, static triaxial tests, and cyclic loading triaxial tests, were performed. The physical properties, shear behavior, and anti-liquefaction strength of the soils were studied in detail. This work aims to investigate the controlling role of the Ta-d pumice on the Iburi landslides by means of mechanical testing and statistical analysis from micro and macro perspectives and further provide a guideline and reference for the disaster mitigation operation in pyroclastic fall deposits.

Geological setting

The southwest Hokkaido, where the Iburi earthquake occurred, is subjected to the northwestward subduction of the Pacific Plate and convergence between the North American and the Eurasian Plates (Kimura 1994; Tamaki et al. 2010). Faults with NNW-SSE and NW-SE strikes are developed in this region. Considerable historical earthquakes have occurred in this region. The Iburi landslides mainly occurred in the hilly terrain at an elevation lower than 350 m and a slope angle less than 30°. The outcropped strata in the Iburi landslide-affected area are dominated by Neogene and Quaternary marine and non-marine sedimentary rocks and Late Pleistocene non-alkaline pyroclastic flow volcanic rocks (Ozaki and Taku 2014).

The Iburi landslides primarily occurred in the pyroclastic fall deposits. The pyroclastic fall deposits (volcanic ash, pumice, and

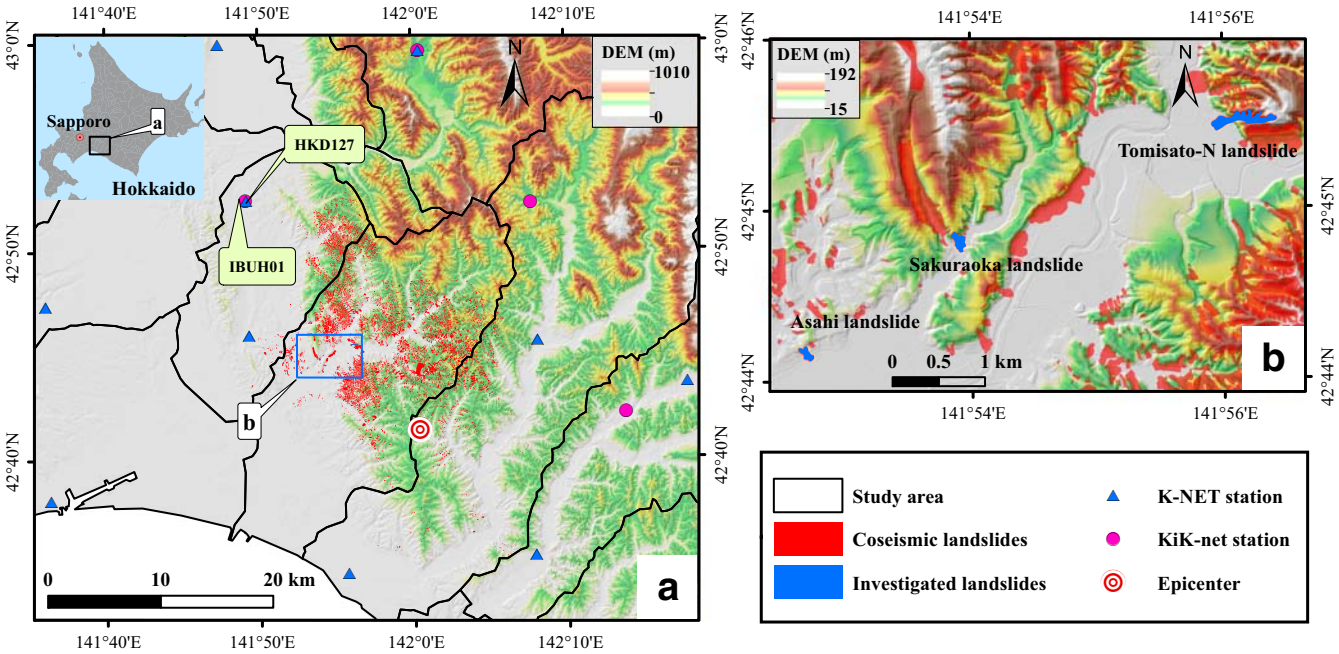

Fig. 1 Location maps. (**a**) Coseismic landslide triggered by 2018 Hokkaido Eastern Iburi Earthquake; (**b**) distribution of three investigated landslides. The Iburi landslide database is derived from Zhang et al. (2019)

scoria) covering the study area mainly originate from Tarumae, Eniwa, Shikotsu, and Kuttara calderas (Yamagata 1994; Osanai et al. 2019). The uppermost deposits in the landslide area are the pyroclastic fall deposits from the Tarumae volcano. Since the study area is distant from the Tarumae volcano, pyroclastic flow deposits can rarely be observed. Based on the eruptive history of the Tarumae volcano, the pyroclastic fall deposits of Tarumae volcano are divided into four layers: the Tarumae a (Ta-a: 1739 AD), Tarumae b (Ta-b: 1667 AD), Tarumae c (Ta-c: 2.5 ka), and Tarumae d (Ta-d: 8.7–10 ka) (Furukawa and Nakagawa 2010; Tajika et al. 2016). Ta-a consists of a mixture of scoria and gray pumice (Tajika et al. 2016). Ta-b is comprised of gray pumice with a clear bedding structure, and the particle size decreases top-down. Ta-c originates from three eruptions around 2.5 ka ago (Furukawa and Nakagawa 2010), and the Ta-c2 from the second eruption layer is widely spread in the landslide area. Ta-c2 is mainly composed of fine-grained gray volcanic ash (Furukawa and Nakagawa 2010). Humus layers are frequently sandwiched in the interfaces between Ta-c and Ta-b as well as Ta-c and Ta-d (Osanai et al. 2019). The Us-b pyroclastic deposits from the nearby Usu volcano and the B-Tm fine-grained pumice from the Baekdu mountain can sometimes be observed between Ta-b and Ta-c in the vicinity of the landslide area. Ta-d is the most widely distributed layer in the study area, and it is composed of two layers, i.e., the upper dark gray coarse scoria (Ta-d1) and the lower porous pumice (Ta-d2). The soil layer underlying the Ta-d layer is the hard and dense silty paleosol with poor permeability. The sliding mass of the Iburi landslide is mainly comprised of the pyroclastic fall deposits mantled on the hard paleosol. In addition, some pyroclastic fall deposits, i.e., Eniwa-a (En-a: 19–21 ka), Shikotsu (Spfa-1 and Spfa-2: 40 ka), and Kuttara (Kt-1: 43.5 ka), originated from the Eniwa and the Shikotsu caldera (Furukawa and Nakagawa 2010), are located between the Ta pumice and the bedrock.

Based on the field investigation, most of the 5625 Iburi landslides (Zhang et al. 2019), except for the 2 deep-seated landslides, are characterized by the overall sliding of the surficial and shallow pyroclastic fall deposits. The sliding zone is located in the Ta-d2 pumice over the hard paleosol. In this work, the isopachs of the pyroclastic fall deposits originating from the Tarumae mountain are depicted in Fig. 2. It should be noted that the isopachs of the pyroclastic fall deposits in Fig. 2 do not strictly and exactly match the thickness and the distribution of the pyroclastic fall deposits in the study area. It was observed in the field survey that the thickness and completeness of the pyroclastic fall deposits vary even in one landslide. Even so, these isopachs can provide a reasonable reference for the analysis of the correlation between pyroclastic fall deposits and the Iburi landslides.

Since the sliding zone of most Iburi landslides was observed in the Ta-d2 pumice during the field work, the correlation between the thickness (isopachs) of Ta-d2 pumice and the Iburi landslide distribution was quantitatively analyzed. An irregular polygon with PGA larger than 5 m/s^2 (Fig. 2) was selected as the targeted area, as the PGA is widely considered as the predominant factor controlling the occurrence of the coseismic landslides (Liao and Lee 2000; Wang et al. 2002; Gorum et al. 2013; Xu and Xu 2014; Xu et al. 2015). A 5-m/s^2 PGA contour was generated based on the PGA map provided by the Quick Estimation System for Earthquake Map Triggered by Observed Records (https://gbank.gsj.jp/QuiQuake/QuakeMap/20180906.en.html). Approximately 98.9% (5561) of the coseismic landslides (5625) are encompassed by the 5-m/s^2 PGA contour. During the quantitative analysis, the targeted area (the irregular polygon) in Fig. 2f is divided into six subareas based on the isopachs of the Ta-d2. These subareas denote the areas with the Ta-d2 thickness of less than 0.08 m, 0.08~0.15 m, 0.15~0.3 m, 0.3~0.5 m, 0.5~1.0 m, and larger than 1 m, respectively. Two terms, landslide area density (*LSAD*) and landslide number

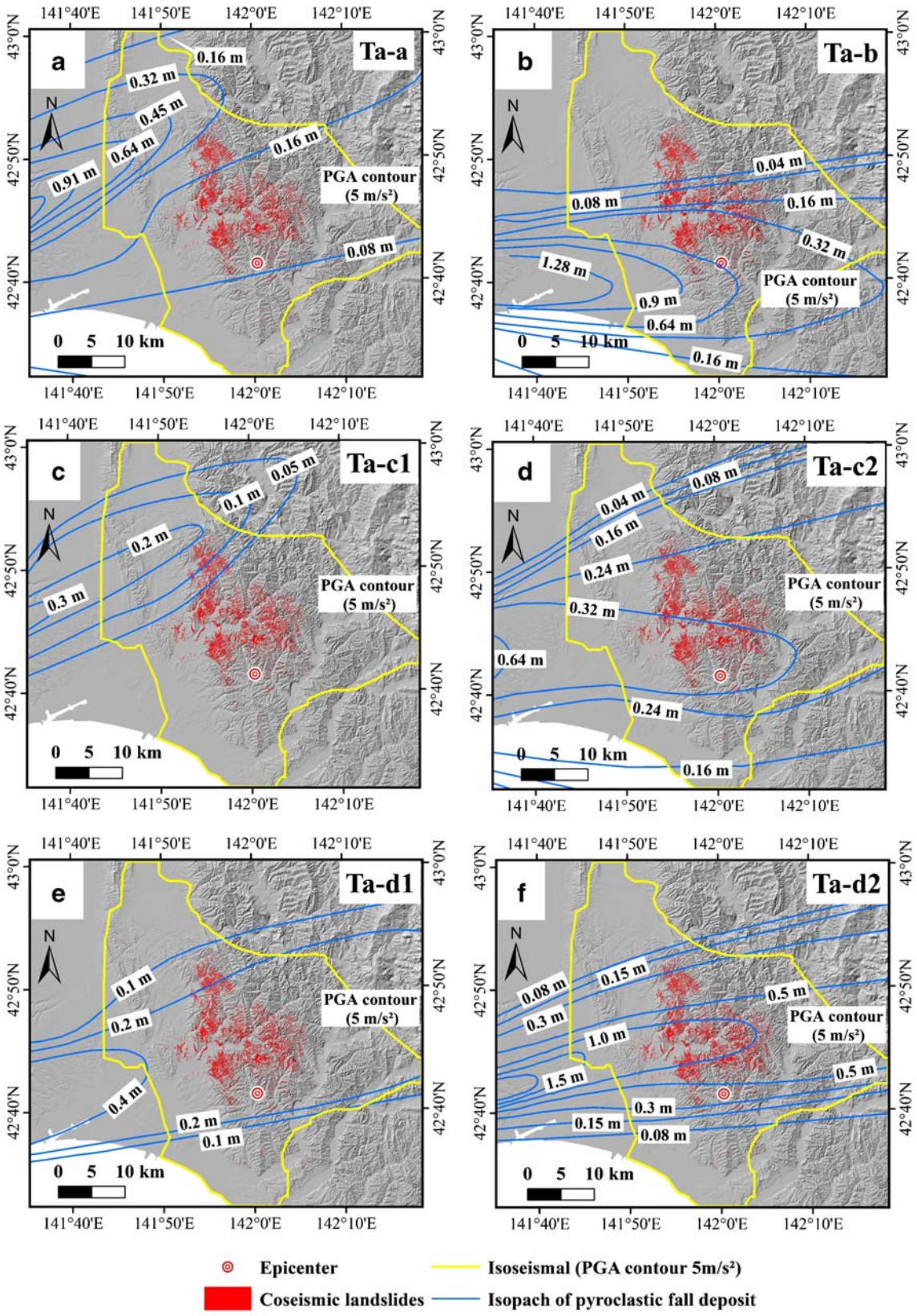

Fig. 2 Isopach maps of the pyroclastic fall deposits ((**a**) Ta-a; (**b**) Ta-b; (**c**) Ta-c1; (**d**) Ta-c2; (**e**) Ta-d1; (**f**) Ta-d2) originated from Mounts Tarumae. The isopachs are based on Furukawa and Nakagawa (2010)

density (*LSND*), are used to describe the density of landslides occurring in each subarea, and the corresponding equations are expressed in Eqs. (1) and (2). Obviously, both the *LSAD* and *LSND* increase with an increase in the thickness of the Ta-d2 pumice despite the subarea with a thickness less than 0.08 m being the largest class (Fig. 3). Moreover, the *LSAD* and *LSND* are very small when the thickness of Ta-d2 pumice is less than 0.15 m. The positive correlation between landslide density and Ta-d2 thickness demonstrates the important role of Ta-d pumice on the occurrence and distribution of the Iburi landslides.

$$LSAD = \frac{LSAP}{\mathrm{CAP}} \times 100\% \quad (1)$$

$$LSND = \frac{LSNP}{\mathrm{CAP}} \times 100\% \quad (2)$$

where *CAP* is the percentage of a certain class (subarea) area to the targeted area, *LSAP* is the percentage of landslide area in a certain subarea to the total landslide area, and *LSNP* is the percentage of landslide number in a certain subarea to the total landslide area.

Types and features of the Iburi landslides

Due to the differences in geomorphology, soil composition and thickness, vegetation, and other affecting factors, the Iburi landslides show diverse geometric features and forms. The landslides can be categorized into two major types (i.e., shallow debris slide and deep-seated landslide) based on the sliding zone location and the sliding mass structure. Only two deep-seated landslides were confirmed, and the rest of the Iburi landslides are mainly shallow debris slides. In this work, the shallow debris slides were regarded as the main objectives, and their typical characteristics were combed out. The shallow debris slides triggered by the Iburi earthquake mainly presented two forms, i.e., translational sliding and mobilization of V-shaped convergent sliding masses. The translational sliding landslide can be further divided into steep translational sliding and gentle translational sliding based on the slope steepness and landslide mobility. Details and representative landslides of these three types of shallow debris slides were described and studied.

Steep translational debris slide

The Sakuraoka landslide (Fig. 1b) is a typical steep translational debris slide, and it is composed of two sub-landslides (Fig. 4). The whole source area is almost exposed due to the displacement of the sliding mass on the steep slope. The alternately bright and dark strips on the exposed planar sliding bed (Fig. 4a) at the upper slope indicate the mobilization direction of the pyroclastic fall deposits. The mean slope angle of the exposed sliding bed along the longitudinal section A-A′ is approximately 22° (Fig. 4b), and the mean slope angle of the exposed sliding bed along the longitudinal section B-B′ gradually decreases from 44° to 10° (Fig. 4c).The apparent mobilized friction angles (Sassa et al. 1996, 2005) for the two sub-landslides are 10.1° and 8.6°, respectively. The sharp bulges near the roads in Figs. 4b, c result from the excavation during the disaster relief operations. According to the field survey and the longitudinal sections, the source area and the deposition area of the Sakuraoka landslide are approximately bordered by the road where the topography changes sharply.

To investigate the soil structure and strength of the Sakuraoka landslide, a series of trenches were dug at the right boundary and along the survey lines (Fig. 4a), and two sets of in situ hardness tests at the main scarp and the right boundary were conducted to obtain the uniaxial compressive strength. The hardness tests were conducted five times for each layer, and the average of the three tests without the maximum and minimum were calculated as the test results. The soil structure and the corresponding uniaxial compressive strength of the Sakuraoka landslide are shown in Fig. 5. At the main scarp of the Sakuraoka landslide (Fig. 5a), the Ta-a pumice and the Ta-b upper coarse pumice were not observed, and the off-white Ta-b fine pumice layer was mantled with the 0.1-m-thick humus. The upper Ta-d layer (Ta-d1) was lost and the total thickness of Ta-d2 layer is approximately 2.45 m. The Ta-d2

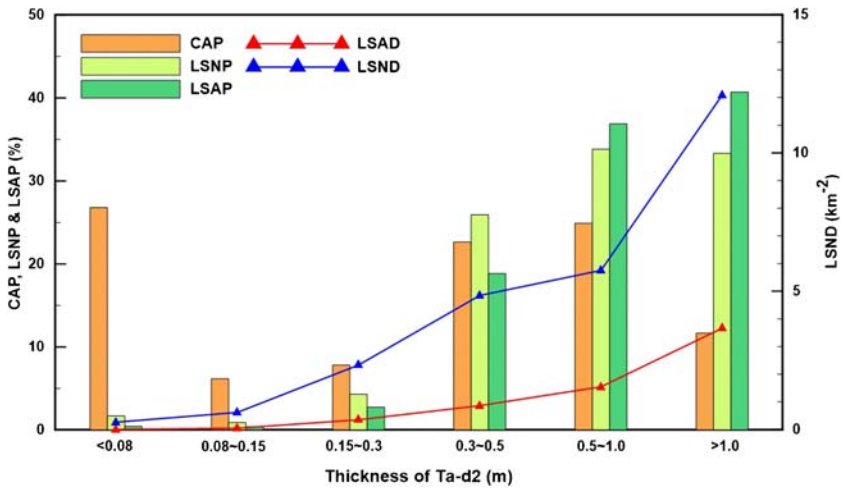

Fig. 3 Relationships between the thickness of Ta-d2 and the occurrence of the Iburi landslides in the corresponding class

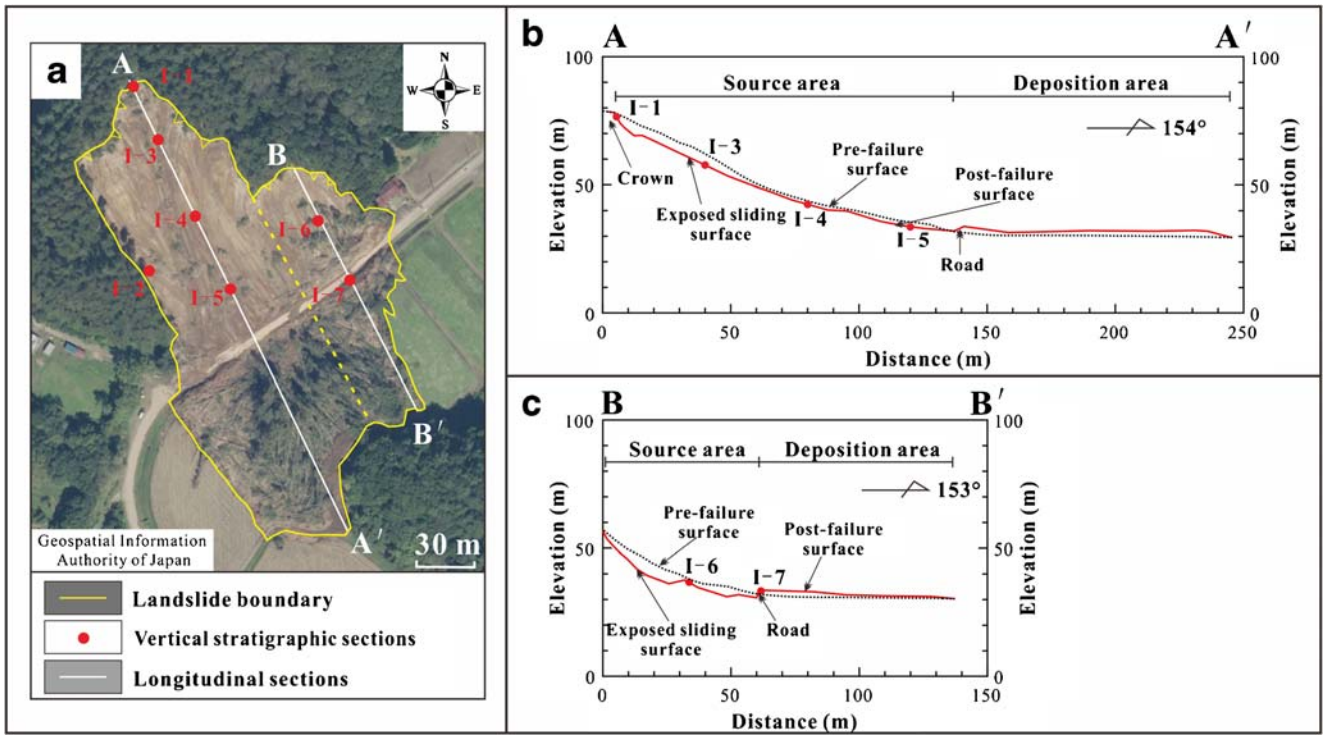

Fig. 4 The typical steep translational debris slide: Sakuraoka landslide. (**a**) General aerial view (the base map is derived from the Geospatial Information Authority of Japan); (**b**) longitudinal section along survey line A-A′; (**c**) Longitudinal section along survey line B-B′

pumice layer was further divided into five distinct sub-layers (Fig. 5a, b) based on the color, particle size, and particle strength. The top sub-layer is brownish-red, and the other four sub-layers are grayish-green. The volcanic ash content of the brownish-red pumice layer (Ta-d pumice with volcanic ash) decreases top-down. The grain size of the upper grayish-green pumice (Ta-d pumice MG) is coarse and decreases sharply at the bottom (Ta-d pumice FG and CS). While the Ta-d pumice FG and CS are the same soil layer in different locations (e.g., sections I-1 and I-2), their properties are different. The particle strength of the Ta-d pumice FG is high, but the Ta-d pumice CS is highly weathered and can be easily crushed with fingers. Several irregularly distributed soft and medium sandy pumice interlayers (Ta-d pumice MS) with different thicknesses can be found in Ta-d, and the water content of the cohesive medium sandy pumice is as high as 144% to 223%. As this Ta-d pumice MS interlayer can be observed in the stable main scrap and flank, it is inferred that the medium sandy pumice may result from the interbedded seepage flow parallel to the slope before the earthquake rather than during the Iburi earthquake. The strength of the pumice layer was reduced due to the long-duration seepage flow, and the pumice layer was eroded and weathered to a powder. The grain strength of the Ta-d pumice is relatively low compared to the Ta-a, Ta-b, and Ta-c layers. The nethermost layer in section I-1 is the silty paleosol, and one dark gray coarse sand layer was observed in the silt layer. However, this coarse sand layer was not observed in other locations of the Sakuraoka landslide. The hardness test results in Fig. 5a show that the uniaxial compressive strength of the pyroclastic fall deposits varies with depth and reaches a minimum value in the Ta-d pumice MS. Then, the uniaxial compressive strength reaches a peak value in the bottom hard silt paleosol.

Figure 6 shows the vertical stratigraphic sections of several points along the survey lines A-A′ and B-B′. In section I-3, the Ta-d pumice are spread on the top with a thickness of approximately 0.05 m, and the middle layer is composed of a mix of crushed pumice and paleosol with a thickness of 0.05 m. The nethermost layer is the off-white and khaki hard paleosol. The soil structures of sections I-4, I-5, and I-6 are almost identical, and both comprise a thin pumice layer at the top and the strong and hard paleosol layer at the bottom. Section I-7 was a profile after the excavation of a buried road near the deposition area. It is inferred that there is no downward erosion during the landslide motion, as the excavated road is sound and the soil integrity is not disrupted. The soil structure of section I-7 closely matches the main scarp and the right flank, and Ta-d pumice is located at the bottom.

Based on the field investigation, the longitudinal sections, and the vertical stratigraphic sections, it is concluded that the Sakuraoka landslide is not a simple collapse of loose pyroclastic fall deposits but rather an integrated motion of the whole pyroclastic fall deposits along the weak layer in Ta-d pumice. The strong ground motion, in combination with the perched groundwater, resulted in the liquefaction in the bottom Ta-d pumice layer and the further motion of whole overlying pyroclastic fall deposits. The scattered pumice remaining on the travel path indicates that the sliding zone was consumed and pinched out.

Gentle translational debris slide

The Asahi landslide is a typical gentle translational debris slide, and the general aerial view and the longitudinal sections are depicted in Fig. 7. According to the field reconnaissance and the longitudinal sections (Figs. 7b, c), the Asahi landslide is characterized by a planar

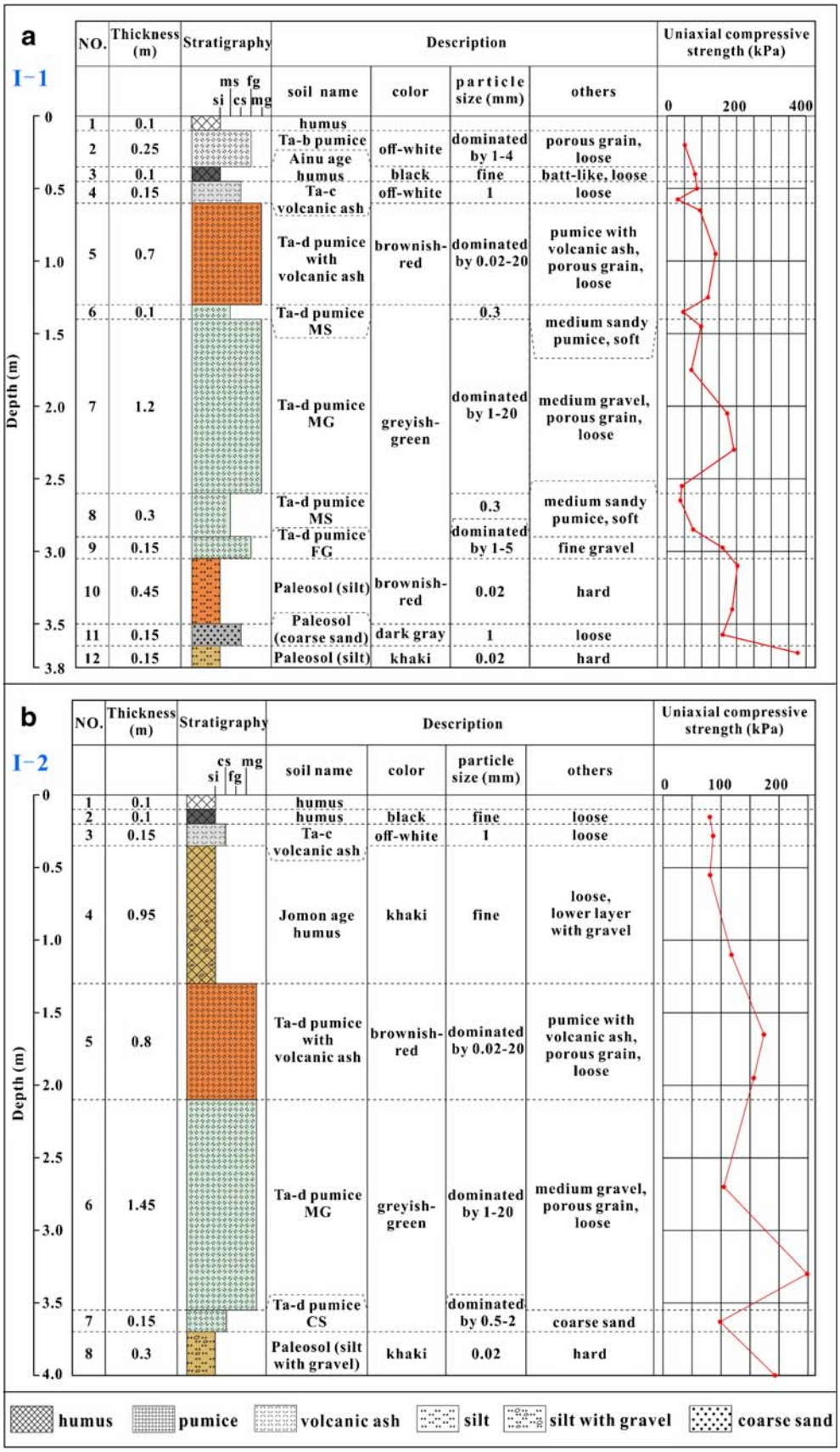

Fig. 5 Stratigraphic columns of the main scarp (**a**) and the right flank (**b**) in the Sakuraoka landslide

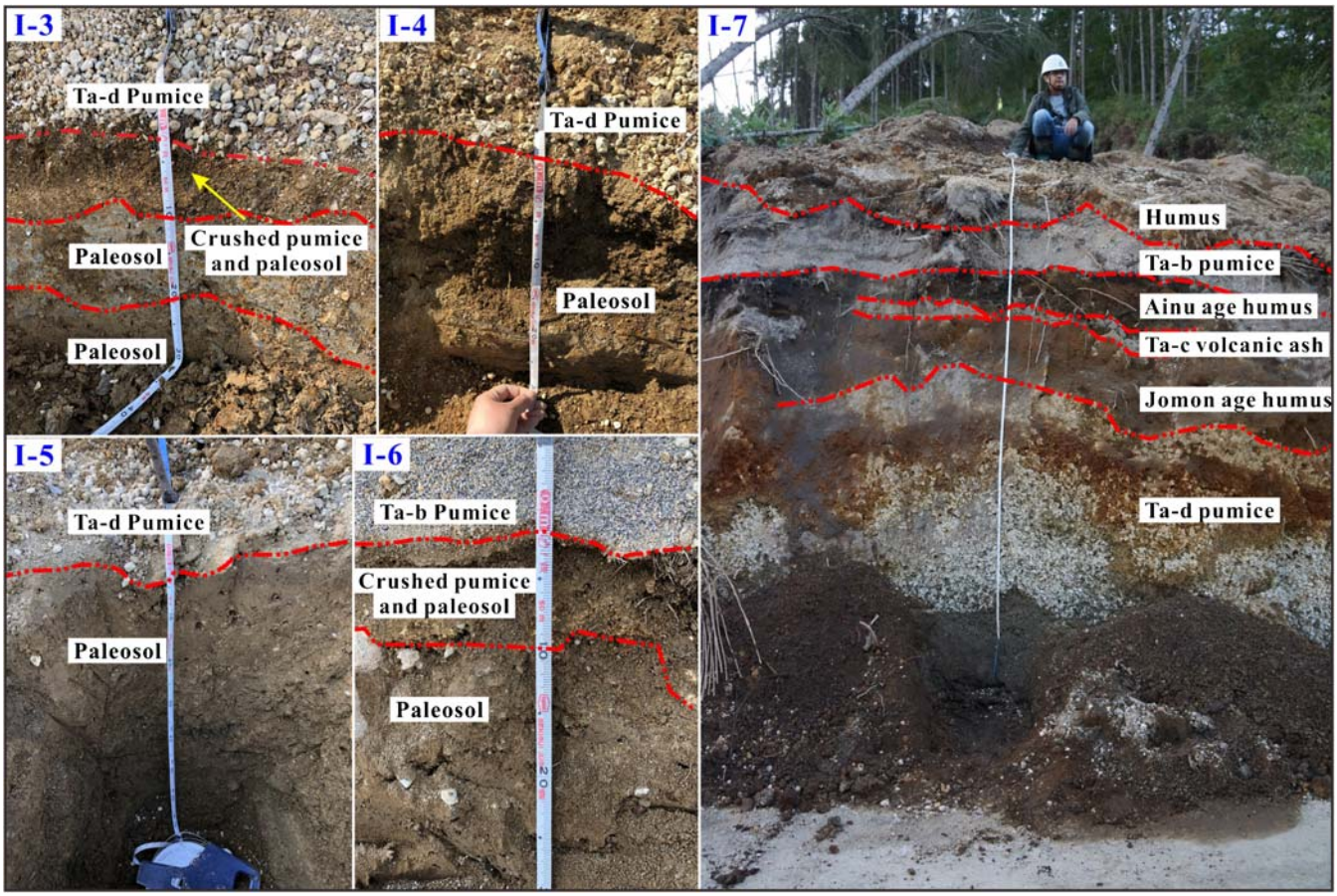

Fig. 6 Vertical stratigraphic sections displaying the soil composition of the sliding zone and the sliding mass in the Sakuraoka landslide. The locations of the sections are depicted in Fig. 4

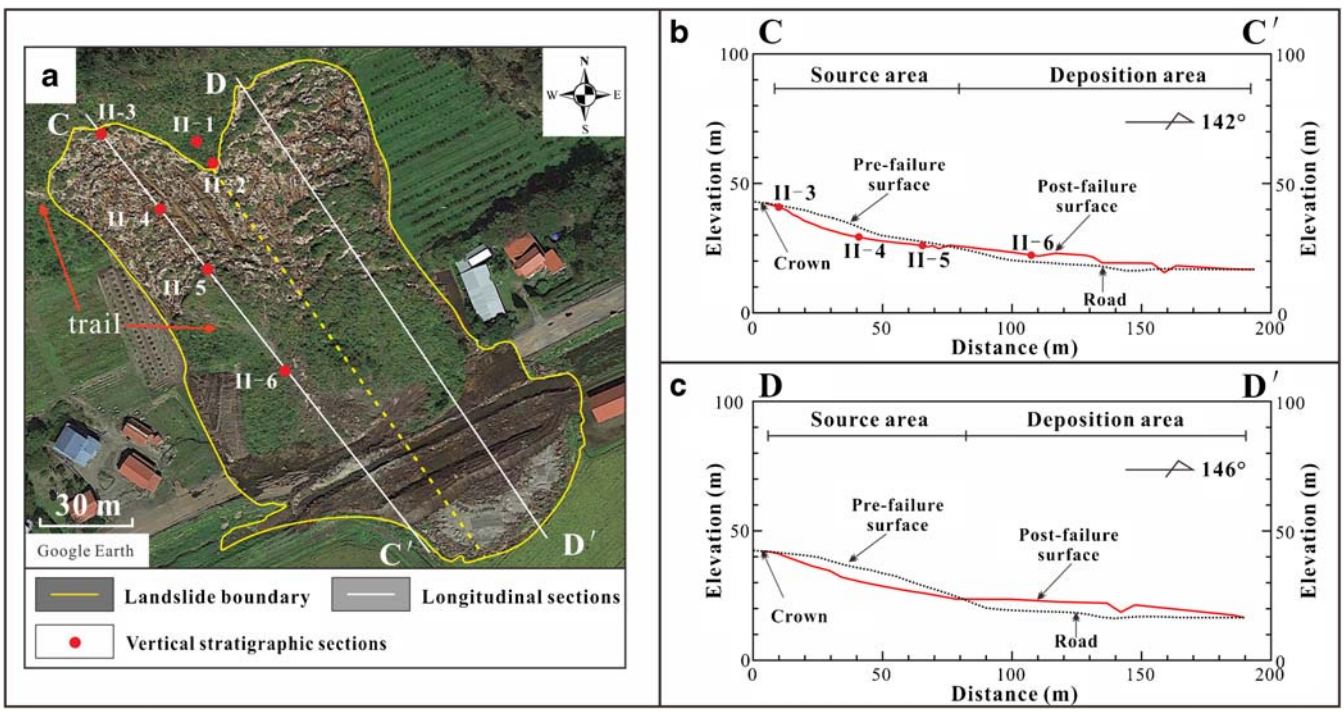

Fig. 7 The typical gentle translational debris slide: Asahi landslide. (**a**) General aerial view (the base map is derived from the Google Earth); (**b**) longitudinal section along survey line C-C′; (**c**) longitudinal section along survey line D-D′

sliding zone and translational downslope motion. The mean slope angle of the source area along the survey line C-C′ is approximately 14°, and the corresponding apparent mobilized friction angle is 7.1°. The mean slope angle of the source area along the survey line D-D′ is approximately 10°, and the corresponding apparent mobilized friction angle is 5.2°. The slope steepness of both sub-landslides of the Asahi landslide is lower than that of the Sakuraoka landslide. The most distinguishing difference between the gentle translational debris slide and the steep translational debris slide is that the sliding zone in the source area is not exposed. Instead, the wavy humus and pumice were seated on the sliding bed at the source area, and the transverse ridges perpendicular to the sliding directions can be easily observed. In the middle of the landslide, an integrated and coherent sliding mass can be clearly noticed (Fig. 7a). In addition, two distinct segments of the mountain trail can be recognized in Fig. 7a. These two segments of trail are confirmed as one mountain trail dislocated by the mass movement, as their widths, trends, and vegetation are nearly identical. Thus, it can be concluded that the sliding mass mobilized as a whole and the integrity as well as the coherence of the sliding mass was not largely destroyed. Controlled by the slope steepness, the movement of the sliding mass at the rear stops and remains on the sliding bed.

Figure 8 shows that the composition and structure of sections II-2 and II-3 are similar to those of the Sakura landslide. The irregular distributed Ta-d pumice MS interlayer can be observed in sections II-2 and II-3. Sections II-4 and II-5 show the sliding mass remaining on the sliding bed. The thickness of each pyroclastic fall deposit layer over the paleosol layer is thinner than that of the corresponding layer at the crown, which demonstrates that the sliding mass at the rear was stretched in the downslope motion. Section II-6 is located in the stable sliding mass at the deposition area, and the soil structure closely matches that at the crown. This means the integrity of the sliding mass remains unchanged. During the field survey, several concrete pieces of the original road that crossed the trench and rested at the landslide toe area were observed. It should be noted that groundwater appeared and perched at a height in the Ta-d pumice layer during the excavation of section II-6 and this also happened 1 day after the excavations of sections II-4 and II-5. This phenomenon was also observed in the investigation of other landslides. Thus, it can be inferred that the groundwater table was very high and almost reached the exposed sliding zone during the Iburi earthquake. The trench excavations of the Asahi landslide were conducted in May 2019, prior to the rainy season (from June to August), while the Iburi earthquake occurred at the beginning of September 2018, just after the rainy season. Therefore, the groundwater table should be very high during the Iburi earthquake, which may have provided the hydrological condition for the widespread liquefaction during the earthquake.

Mobilization of V-shaped convergent sliding masses

The Tomisato-N landslide is a typical mobilization of V-shaped convergent sliding masses occurring in rugged valley terrain. The longitudinal section (Fig. 9b) was measured almost along the valley line, and the slope angle is approximately 15°. The slope angles of the cross sections (Fig. 9c) range from 20° to 40°. This type of landslide constitutes a set of sub-landslides. Clear strips parallel to the sliding direction can be observed on the exposed sliding bed of the sub-landslides. In this light, it is similar to the translational debris slides. A series of convergent-sliding sub-landslides provided the provenance and source for the further mobilization in the valley. The disrupted sliding mass along with the stream in the valley formed

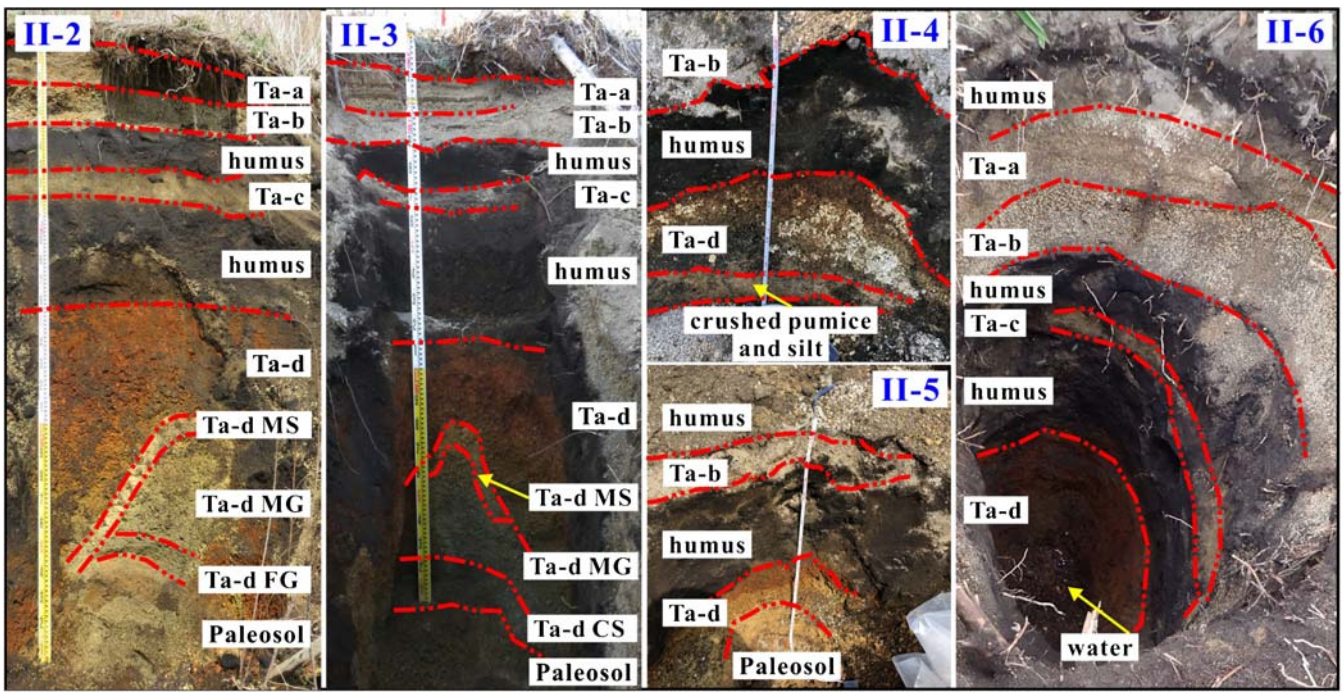

Fig. 8 Vertical stratigraphic sections displaying the soil composition of the sliding mass in the Asahi landslide. The locations of the sections are depicted in Fig. 7

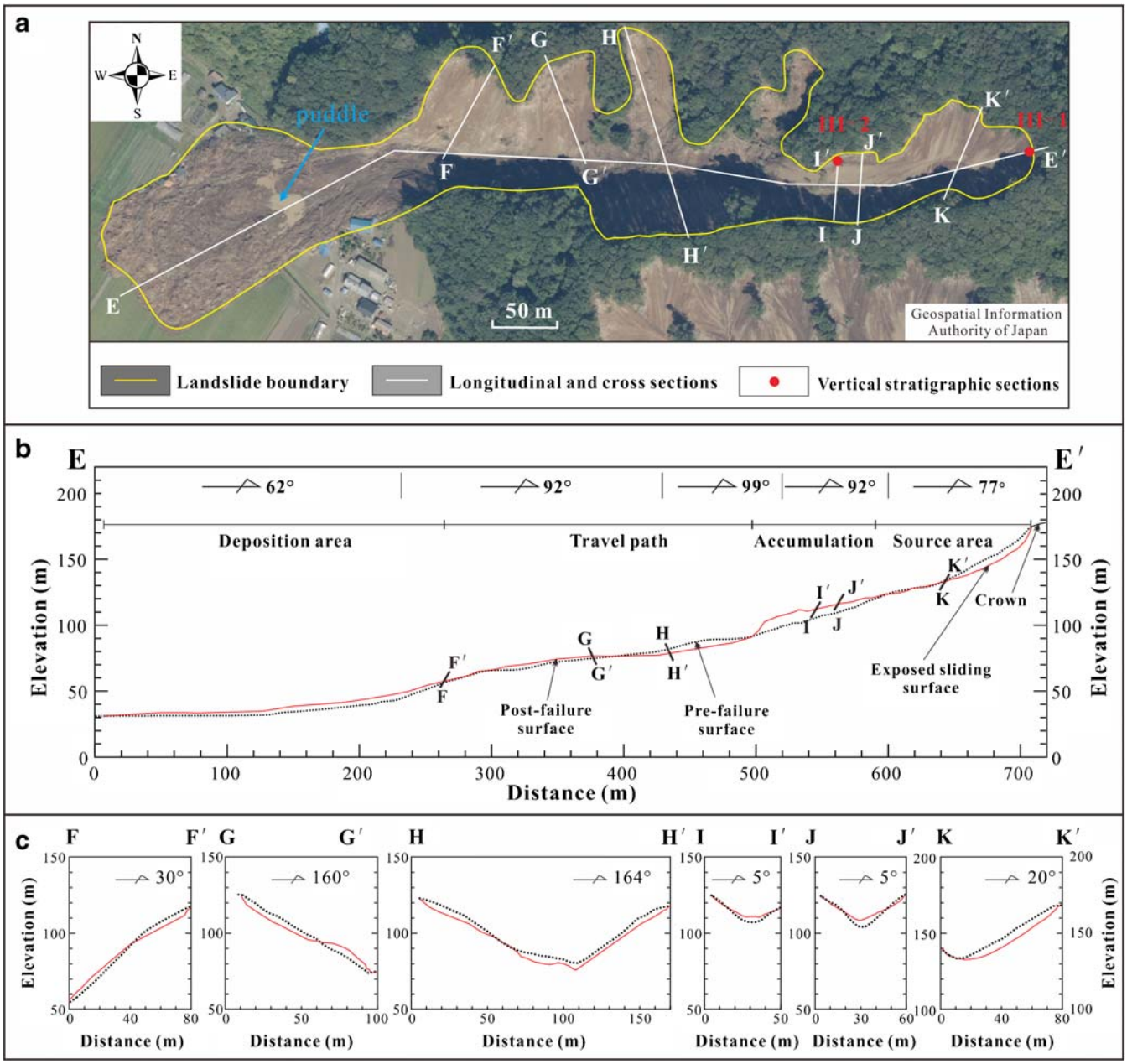

Fig. 9 The typical mobilization of V-shaped convergent sliding masses: Tomisato-N landslide. (**a**) General aerial view (the base map is derived from the Geospatial Information Authority of Japan); (**b**) longitudinal section along survey line E-E′; (**c**) Cross sections along survey lines F-F′, G-G′, H-H′, I-I′, J-J′, and K-K′

the flow-like landslide and rushed down to the ditch outlet. A soft disrupted sliding mass was observed on the travel path, and no integrated sliding block was found in this type of landslide. Several puddles can be observed in the deposition area (Fig. 9a). The soil in the deposition area was very soft, and people could be easily trapped, as in swamps. This means that the water content and the groundwater table were high during the earthquake.

In the Tomisato-N landslide, the vertical stratigraphic sections at the main scarp and the right flank are similar to those of the Sakura landslide and Asahi landslide. In the right flank, the paleosol layer can be traced to the paleosol layer in the exposed sliding bed, which demonstrates that the sliding zone is localized in the Ta-d pumice layer overlying the stable and hard paleosol layer.

Summarization of the failure mode

In this section, three main types of the coseismic landslides were classified, and their failure modes were described in detail. Generally, localized liquefaction occurred in the weak layer of the Ta-d pumice during the strong ground motion, and the integrated sliding failure occurs in the initiation stage. Then, the whole sliding mass mantled on the liquefied layer moves downslope. In the motion stage, controlled by the topography and other factors,

three mobilization types (steep translational sliding, gentle translational sliding, and the mobilization of V-shaped convergent sliding masses) appeared.

Geotechnical properties and triaxial test results

Geotechnical properties

The soil composition of the landslides is a predominant factor controlling landslide occurrence. It is important to understand soil properties to investigate the failure mechanism of the landslides (Gratchev and Towhata 2010; Wiemer et al. 2015). To investigate the geotechnical properties of the soil layers, a set of in situ and laboratory tests were conducted, and the in situ density (ρ), dry density (ρ_d), water content (w), specific gravity (Gs), void ratio (e), and degree of saturation (S_r) were obtained. The ρ, w, e, and S_r were tested using the undisturbed samples. The undisturbed samples applied in the tests were taken from the main scarp of the Asahi landslide, and all the tests were performed following the standards of the Japanese Geotechnical Society (JGS 2010). The test results are summarized in Table 1. As the specific gravities of different pumice particles vary with the grain size, porosity, and structure, the Gs of pumice layers in Table 1 were the results of the triturated samples. In fact, the Gs of some pumice samples are smaller than 1. As illustrated in Table 1, the S_r of the paleosol (silt) and the Ta-d pumice MS are very high, and the w of the Ta-d pumice MS is very high as well. The ρ_d of the Ta-d pumice layers are relatively low due to their large porosity. These tested parameters are used in soil classification, and they are adopted in preparation of remolded samples in the triaxial tests.

Considering most Iburi landslides are translational sliding along the interface between the Ta-d pumice and the hard paleosol, soils located around the sliding zone (i.e., the Ta-d pumice layers and the paleosol layer) are regarded as the focus of this study. Figure 10 shows the grain size distributions of the soils from the main scarp of the Asahi landslide. The Ta-d pumice FG and the Ta-d pumice CS are taken from the vertical sections II-2 and II-3 (Fig. 7a), respectively. Although these two samples are from the same soil layer at different localities, their grain size distributions have significant differences. The content of fine-sized particle (less than 0.075 mm) in Ta-d pumice CS is higher than that in Ta-d pumice FG, and the grain strength of Ta-d pumice CS is lower than that of Ta-d pumice FG. The Ta-d pumice MS and the paleosol (silt) layer contain not only a high percentage of fine-sized particles but also a low percentage of coarse-sized particles. Thus, the uniformity coefficients (C_u) for these two layers are large, and the coefficients of curvature (C_c) are small (Table 2). The paleosol layer is abundant in clay and fine-sized particles, and the clay and fine-sized contents are as high as approximately 35% and more than 60%, respectively. While the dry density is small, this paleosol layer maintains a low permeability. Based on the grain size analysis, the Ta-d pumice MS is defined as medium sand. This layer comprises weathered pumice powder, black sand, and a handful of intact pumice particle. The strength of the black sand is high while the strength of the intact pumice particle being low.

Consolidated-undrained static triaxial compression test

The consolidated-undrained static triaxial compression test is commonly employed to investigate the strength properties of soil (Wang et al. 2015; Yang et al. 2015a; Xu et al. 2018). The friction coefficient as well as the stress-strain behavior of soil during the deformation process can be obtained from the stress-strain relationship and the stress path curve. In the tests, remolded samples were used, and the dry density of the remolded specimens before consolidation was controlled to be same with the undisturbed soils. The dried samples were filled into a cylindrical rubber membrane to obtain a remolded specimen with a height of 100 mm and a diameter of 50 mm. To ensure that the grain size of the samples is less than 10% of the specimen diameter, only samples passing through the 4.75-mm sieve was used. Carbon dioxide was slowly supplied from the base of the specimen to exhaust the air completely, and the de-aired water was thereafter supplied to the specimen gradually. Then, Skempton's B value (Skempton 1954; Ortigao 1995) was obtained to check the degree of saturation of the specimens. Skempton's B values of all the specimens used in this work were higher than 0.95, and the specimens were considered fully saturated (Sassa 1985; Tokimatsu et al. 1990; Yang et al. 2015b). Lastly, the specimens were consolidated under certain confining stress (σ_0'). After the specimen consolidation, the specimens were compressed with an axial strain of 1.0% per minute under undrained conditions. The axial stress increment ($\Delta\sigma_1 = \sigma_1\text{-}\sigma_0'$) and

Table 1 Physical properties of the soil samples from the crown of the Asahi landslide

Soil layer	ρ (kg/m^3)	ρ_d (kg/m^3)	w (%)	G_s	e	S_r (%)
Surface humus	1258	1083	16.2	2.653	1.451	29.7
Ta-a pumice	1249	1065	17.2	2.733	1.565	30.1
Ta-b pumice	909	693	31.2	2.641	2.813	29.3
Black humus	1083	540	101	2.528	3.684	69.1
Ta-c pumice	1333	1086	22.8	2.769	1.550	40.8
Ta-d pumice with volcanic ash	1122	506	121	2.553	4.041	76.7
Ta-d pumice MG	874	281	210	2.542	8.029	66.6
Ta-d pumice FG	891	530	68.1	2.624	3.950	45.2
Ta-d pumice CS	1023	511	100	2.627	4.141	63.6
Ta-d pumice MS	1177	385	206	2.631	5.842	92.8
Paleosol (silt)	1649	1028	60.4	2.735	1.660	99.5

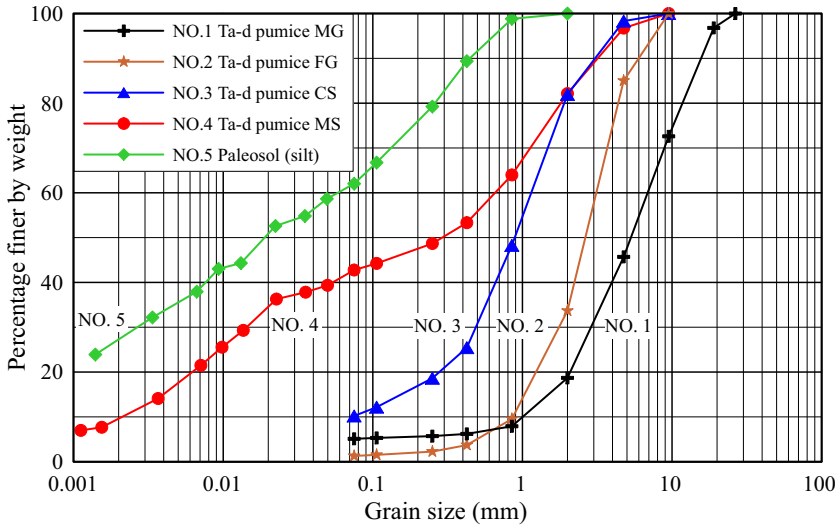

Fig. 10 Grain size distributions of the samples from the main scarp (II-2 and II-3 in Fig. 7) of the Asahi landslide

pore water pressure (u) data were obtained. Consolidation pressures of 30 kPa, 40 kPa, and 50 kPa were selected based on the soil thickness and soil density of the aforementioned vertical sections.

Figure 11 shows the stress-strain relationships of the saturated specimens in the consolidated-undrained tests, and only the test results with a confining stress of 40 kPa were depicted. The general trends of the axial stress increment and the pore water pressure of Ta-d pumice MG (No. 1 in Fig. 11) and Ta-d pumice FG (No. 2 in Fig. 11) are similar. The pore water pressures of both specimens increase rapidly with an increase in the axial strain, and the specimens are mainly compacted at this stage. When the axial strain reaches approximately 3%, the pore water pressure reaches a peak value, and the increment of the pore water pressure is larger than 1/3 of the axial strain increment. This means excess pore water pressure is generated at this stage (Skempton 1954; Ortigao 1995). Then, with the continuous increase of the axial strain, the specimen changes from a contractive state to a dilative state to overcome the shear resistance between particles, and the pore water pressure decreases accordingly. The axial stress increment increases with an increase in the axial strain to a large value, indicating the strain hardening of the two types of pumice specimens.

The behavior of the Ta-d pumice CS (No. 3 in Fig. 11) in the consolidated-undrained triaxial tests is quite different from those of the Ta-d pumice MG and the Ta-d pumice FG. The axial stress increment and the pore water pressure increase with the increase in the axial strain and then remain stable. Only contractive behavior is observed for the Ta-d pumice CS. The peak value of the axial stress increment is 36.4 kPa, which is far less than the peak values of the Ta-d pumice MG and the Ta-d pumice FG. This phenomenon results from the specimen particle being crushed under increased axial strain. To justify the occurrence of grain crushing, grain size analysis of the Ta-d pumice FG and the Ta-d pumice CS after the test was conducted as well. As depicted in Fig. 12, the grain size distribution curve of the Ta-d pumice FG after the test is similar to before test, while the grain size distribution curve of the Ta-d pumice CS after the test deviates remarkably to the left. The considerable increase in the fine particles (left deviation) of the Ta-d pumice CS indicates that grain crushing must have occurred during the compression tests. Figure 13 shows the stress-strain relationship and stress path of the remolded specimen from the Ta-d pumice FG. The grain size distribution of the remolded specimen was conditioned to be consistent with that of the Ta-d pumice CS. The general trends of the axial stress increment and the pore water pressure of the remolded specimen are similar to those of the Ta-d pumice FG, but the peak value of the axial stress is smaller. Thus, the grain crushing phenomenon is considered to control the stress-strain behavior of Ta-d pumice CS. The grain crushing inhibits the occurrence of dilation and strain hardening. Similar phenomena have also been observed in previous studies (Sassa et al. 1996; Wang 1999).

Table 2 Grain size distributions, CSL equations, and failure criterion equations of the samples around the sliding zone

Layer name	D_{50} (mm)	C_u	C_c	CSL equation	Failure criterion equation
Ta-d pumice MG	5.2	6.9	1.1	$t = 0.81\ s'$	$\tau = 1.38\ \sigma'$
Ta-d pumice FG	2.4	3.6	1.1	$t = 0.75\ s'$	$\tau = 1.13\ \sigma'$
Ta-d pumice CS	0.89	15	3.0	$t = 0.57\ s' + 5.8$	$\tau = 0.69\ \sigma' + 7.1$
Ta-d pumice MS	0.29	3.0×10^2	0.13	$t = 0.58\ s' + 2.0$	$\tau = 0.71\ \sigma' + 2.5$
Paleosol (silt)	0.019	1.2×10^2	0.21	$t = 0.50\ s' + 2.2$	$\tau = 0.58\ \sigma' + 2.5$

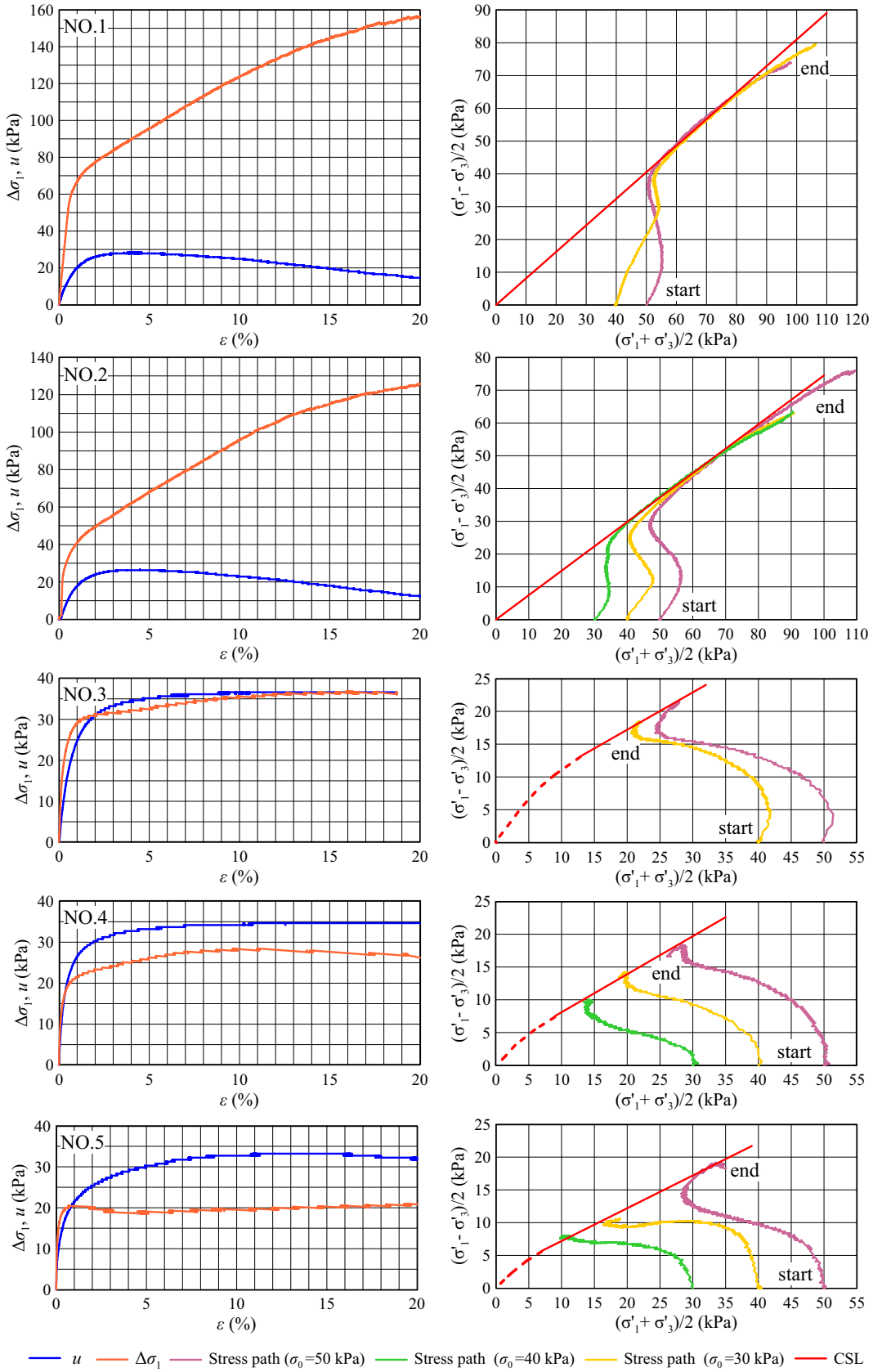

Fig. 11 Stress-strain relationships under the confining pressures of 40 kPa (left) and effective stress paths (right) of the saturated specimens in the consolidated-undrained triaxial compression tests

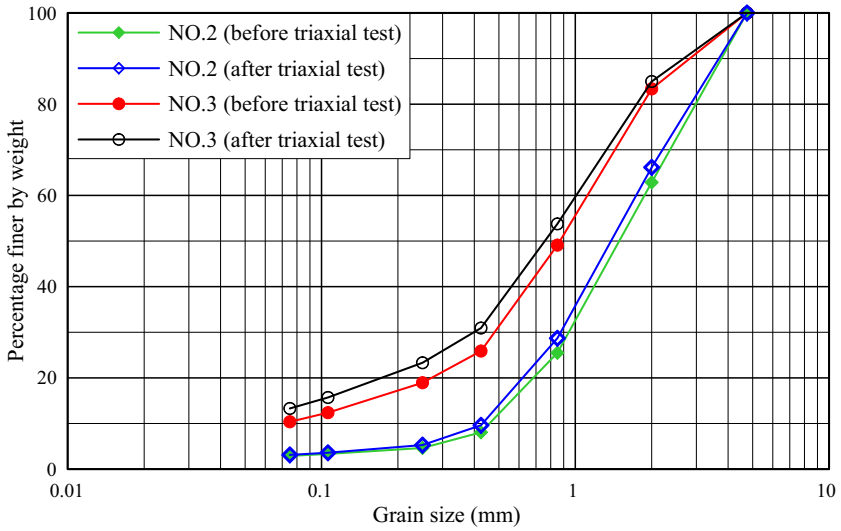

Fig. 12 Grain size distributions of two specimens before and after the consolidated-undrained triaxial compression test

The axial stress increment of the Ta-d pumice MS (No. 4 in Fig. 11) first increases with an increase in the axial strain and then decreases. The peak axial stress increment is 28.4 kPa. The axial stress increment of the paleosol specimen (No. 5 in Fig. 11) reaches its peak when the axial strain is approximately 1%, while the pore water pressure is still slowly increasing. The pore water pressures of the Ta-d pumice CS, the Ta-d pumice MS, and the paleosol is approximately equal to the confining stress, indicating that static liquefaction occurs in all these specimens. However, the pore water pressure of the Ta-d pumice MS clearly increases much faster than that of the paleosol specimens. This phenomenon can be also observed in the cyclic loading triaxial tests. Thus, it could be concluded that the Ta-d pumice MS is more susceptible to liquefaction than paleosol.

For the remolded specimens with normal consolidation, the cohesion obtained in consolidated-undrained triaxial compression tests is positively correlated with the consolidation pressure. The obtained cohesion in triaxial test will be 0, when the consolidation pressure is 0. Thus, the critical state line (CSL) passes through the origin in general. In addition, as the cohesion and the friction angle of soil are difficult to be clearly differentiated (Li 2004), the cohesion and the friction angle were considered as a whole (shear strength), and only the shear strength of specimen was presented in this work. The equations for the CSL and the failure criterion equations of the five layers are summarized in Table 2. The shear strength of both the paleosol layer and the Ta-d pumice layers is high, which explains why the pumice slope can remain stable in a natural state while the cohesion of the loose pumice is very low. The static shear strength of the five layers is positively correlated with the grain size, i.e., the shear strength of the Ta-d pumice MG is the largest, while the shear strength of the Ta-d pumice MS and the paleosol is relatively low. The stress paths of the Ta-d pumice MG and the Ta-d pumice FG move toward the upper right side along the CSL after reaching the CSL. This implies that strain

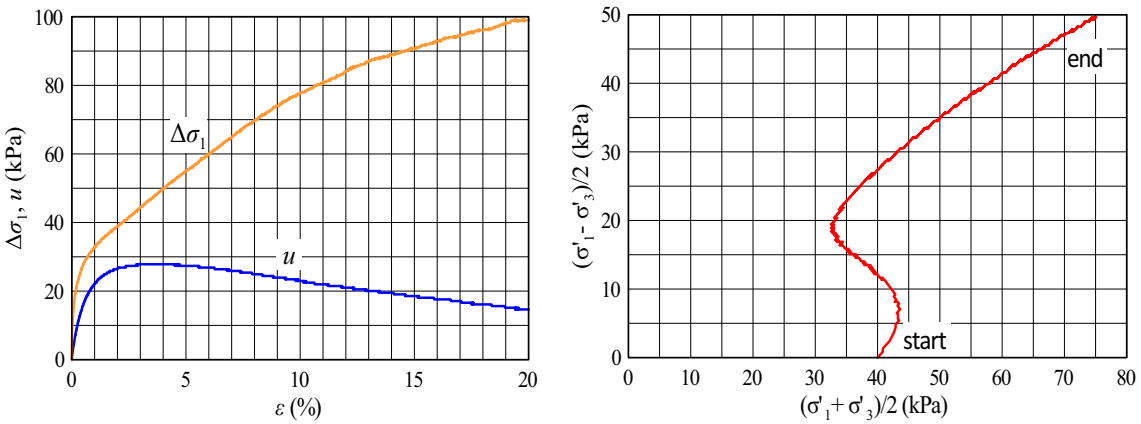

Fig. 13 Stress-strain relationship under the confining pressures of 40 kPa (left) and effective stress path (right) of the remolded specimen from Ta-d pumice FG; the grain size distribution of the remolded specimen was conditioned to be consistent with that of the Ta-d pumice CS

hardening occurs in these specimens. The stress path of the Ta-d pumice MS shows a lower-left trend after reaching the CSL.

Consolidated-undrained cyclic loading triaxial tests

Soil liquefaction resulting from strong ground motion has been an important topic in geotechnical earthquake engineering since the 1964 Alaska and Niigata earthquake (Fukuoka 1966; Seed 1968; Scott and Zuckerman 1972; Takch et al. 2016). Shallow slope failures triggered by strong earthquakes are commonly related to cyclic liquefaction in soil (Seed 1968; Ishihara et al. 1990; Harp et al. 2003; Pei et al. 2017). To study the anti-liquefaction strength of the soils around the sliding zone under seismic loading, a set of stress-controlled cyclic loading triaxial (CTX) testing were performed. The same specimen preparation procedure applied in the static triaxial test was utilized in the CTX tests. During the cyclic loading, stress variation on a plane dipping at 45° is exploited to simulate the cyclic shear stress applied to the soil in the earthquake. To maintain constant normal stress on the 45°-dipping plane, the confining stress should be corrected. Considering that only the pore pressure is affected by the variation of the confining stress, the corrected pore pressure ratio (r_u) was used to describe the variation in the pore water pressure (Zlender and Lenart 2005; Xie 2011; Faris and Wang 2014). The corrected pore water pressure ratio is defined in Eq. (3).

$$r_u = \frac{\Delta u - \frac{\Delta\sigma_1}{2}}{\sigma_o'} \tag{3}$$

where Δu is the increment of pore water pressure and σ_o' is the effective isotropic consolidation stress.

The anti-liquefaction strength of soil is commonly evaluated by the relationship between the cyclic shear stress (τ_d) and the number of cycles required for liquefaction (N_L). The N_L when liquefaction occurs ($r_u = 1$) could be determined by the variation curves of the pore water pressure ratio. Under identical consolidation conditions, multiple sets of N_L with different σ_d can be obtained by changing the dynamic stress σ_d. The cyclic shear stress is calculated using Eq. (4). Then, the correlation between the cyclic shear stress ratio ($\frac{\tau_d}{\sigma_o'}$) and the logarithm of N_L ($\log N_L$) can be obtained (Seed et al. 1975). In this work, the confining stress applied in the CTX test is 40 kPa. A sinusoidal cyclic axial load was applied in the test at a frequency (f) of 1.5 Hz under an undrained condition. The various dynamic stresses exerted on the specimens and their corresponding N_L were listed in Table 3.

$$\tau_d = \frac{1}{2}\sigma_d \tag{4}$$

Table 3 Results of the consolidated-undrained cyclic loading triaxial test for the samples around the sliding zone

Layer name	σ_d (kPa)	τ_d/σ_o'	N_L
Ta-d pumice FG	29	0.36	44
	28	0.35	109
	23	0.29	1115
Ta-d pumice CS	27	0.34	29
	23	0.29	46
Ta-d pumice MS	25	0.31	27
	21	0.26	78
	10	0.13	1386
Paleosol (silt)	28	0.35	41
	21	0.26	581
	10	0.13	2881

The variation curves of the axial stress increment, the axial strain increment, and the pore water pressure ratio with the number of loading cycles (N) of Ta-d pumice CS are illustrated in Fig. 14. As N increases, the ability to resist loading gradually decreases. Thus, the amplitude of the axial stress variation reduces and stabilizes at a relatively low value finally. The amplitude of the axial strain variation increases with an increase in N. The pore water pressure varies with the cyclic loading, and excess pore water pressure is generated. The excess pore water pressure rises continuously and is approximately equal to the confining stress. Thus, liquefaction occurs in the Ta-d pumice CS specimen. The stress paths (Fig. 15) present the cyclic mobility behavior of Ta-d pumice CS in the CTX test. The pore water pressure rapidly increases initially and reaches a stable state in the following cycles. The correlations between $\frac{\tau_d}{\sigma_o'}$ and $\log N_L$ of specimens are illustrated in Fig. 16. The liquefaction resistance of the four soil layers is further concluded as follows: Ta-d pumice MS < Ta-d pumice CS < Paleosol (silt) < Ta-d pumice FG.

Correlation between the Ta-d pumice and the Iburi landslide occurrence

In this work, field investigations were performed in detail to investigate the soil composition, sliding zone, and failure mechanism of the coseismic landslides. Three types of landslides were confirmed, and all three types of landslides shared the same initiation feature, i.e., the global motion of the soil mass along the zone at the Ta-d layer. Meanwhile, in situ and laboratory tests were conducted to investigate the shear behavior and the anti-liquefaction strength of the pyroclastic fall deposits. The test results indicate that the Ta-d pumice MS with a D_{50} of 0.3 mm and the Ta-d pumice CS with a low particle strength have a lower anti-liquefaction strength than the other layers of soil. In addition, the dilative behavior and strain-hardening behavior observed in Ta-d pumice FG raise the bar for the occurrence of shear failure and liquefaction. A stable interbedded paleosol layer was developed between the deposition of the underlying En-a pumice (19–21 ka) and the superjacent Ta-d pumice (8.7–10 ka). The fine-grained paleosol retains low permeability, and the perched groundwater could maintain a certain level above the paleosol layer. Meanwhile, seepage flow could develop over the paleosol layer, which enhances the soil erosion of the lower Ta-d pumice. In fact, the Ta-d pumice MS and fragile Ta-d pumice CS were extensively observed in the Ta-d pumice. The existence of the medium sandy or fragile pumice layers heightens the liquefaction potential of the Ta-d pumice and further encourages the landslide risk under intense ground motion. Therefore, it is concluded that the widespread occurrence of the Iburi landslides results from the localized liquefaction of the medium sandy Ta-d pumice MS or fragile Ta-d pumice CS layers under earthquake motions. In addition, the positive correlation between Iburi landslide distribution and Ta-d pumice thickness was analyzed on macroscale. These results

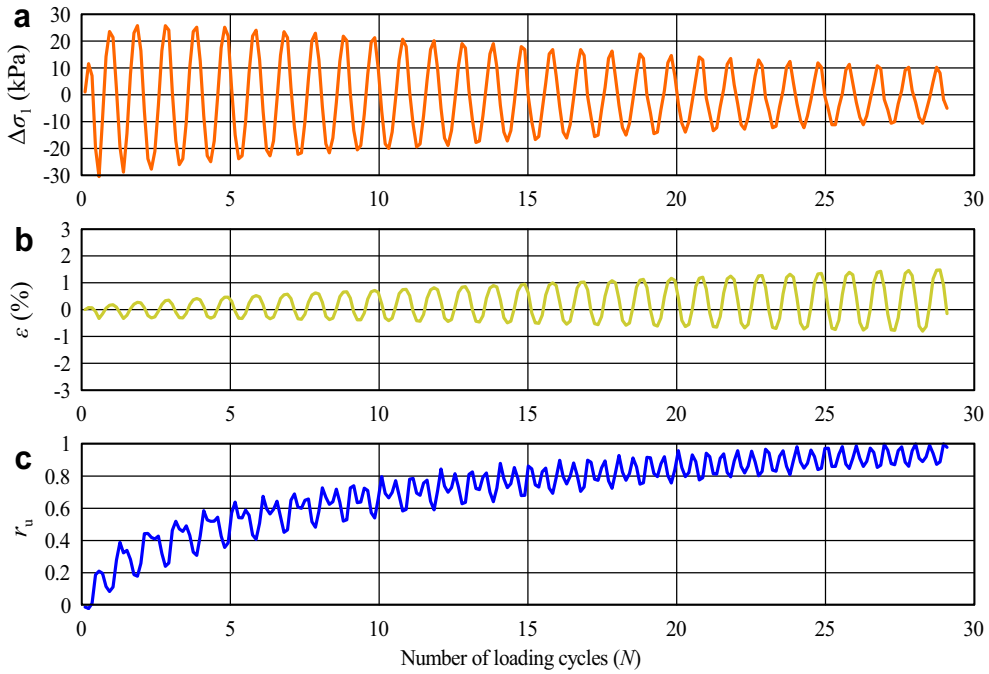

Fig. 14 Correlations between the axial stress increment ($\Delta\sigma_1$) (**a**), the axial strain increment (ε) (**b**) and the pore pressure ratio (r_u) (**c**) with the number of loading cycles (N) of Ta-d pumice CS

emphasize the key controlling role of the Ta-d pumice on the occurrence of the Iburi landslides.

The historical earthquakes that occurred in the landslide distribution area and its vicinity were collated. The 2017 M_w 5.3 earthquake occurred in the Iburi landslide distribution area, and another five earthquakes (the 2009 M_w 5.5 earthquake, the 2007 M_w 5.5 earthquake, the 1981 M_w 6.3 and M_w 5.0 earthquakes, and the 1978 M_w 5.0 earthquake) occurred less than 20 km from the landslide affected area. The largest PGA of the historic earthquakes in the vicinity of the 2018 Iburi landslide area was 3.34 m/s^2 in the 2017 M_w 5.3 earthquake, recorded in the IBUH01 KiK-net station (Fig. 1a). None of these historic earthquakes triggered massive landslides. As most Iburi landslides occurred in the area with the PGA larger than 5 m/s^2, it could be inferred that there is high potential for the substantial

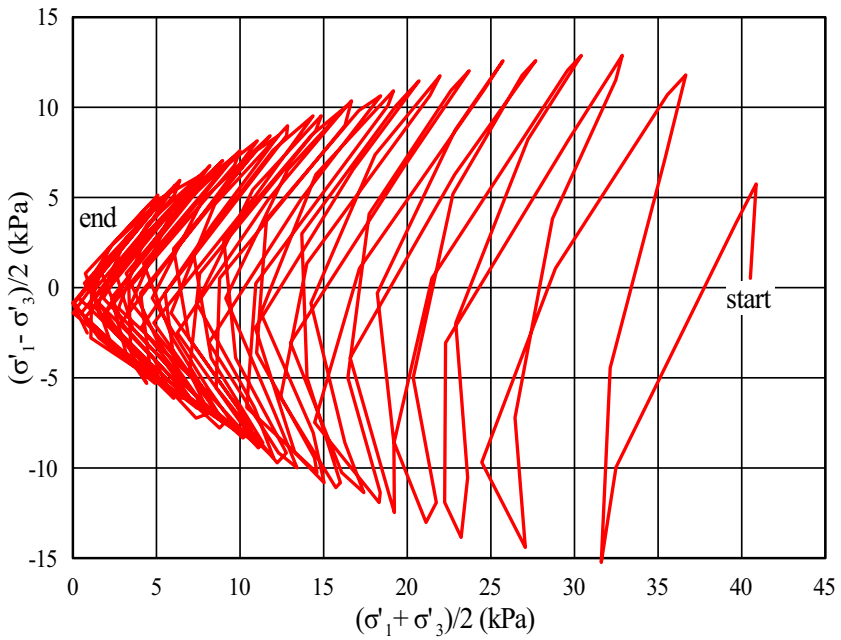

Fig. 15 Effective stress path of Ta-d pumice CS during the consolidated-undrained cyclic loading triaxial test

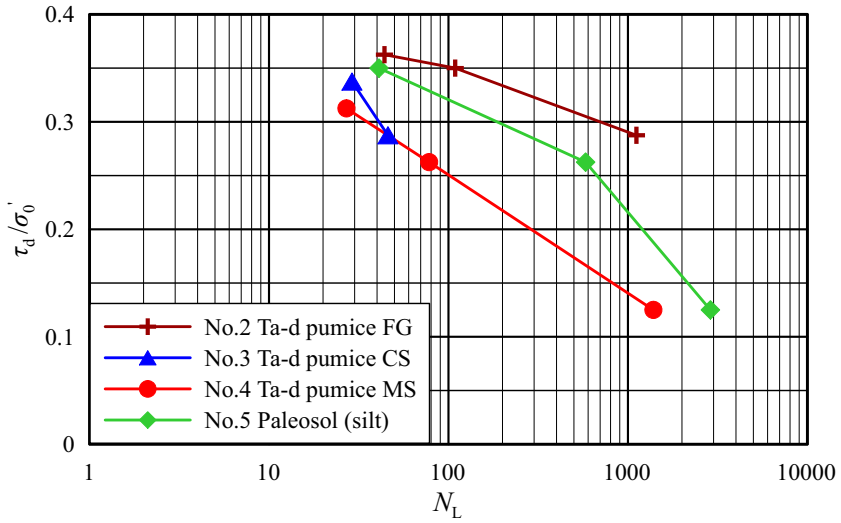

Fig. 16 Correlations between the cyclic shear stress ratio ($\frac{\tau_d}{\sigma_0'}$) and the number of cycles required for liquefaction (N_L)

occurrence of landslides in this area when the PGA is larger than 5 m/s^2. The strong ground motion along with the existence of the widely deposited Ta-d medium sandy pumice and Ta-d fragile pumice is concluded to be the foremost factors responsible for the destructive Iburi landslides. This study can provide a guideline for future disaster mitigation operations for this area and a reference for similar area covered by strong-weathered pumice.

Conclusions

A succession of field investigations, statistical analysis, and laboratory tests were implemented to scrutinize the controlling role of the Ta-d pumice on the massive occurrence of the Iburi landslides. Based on the longitudinal and vertical stratigraphic sections, the types of the Iburi landslides are classified in detail and the initiation, and motion features of different types of landslide are elaborated. Both in situ tests and laboratory tests were conducted, and the physical properties, shear strength, and anti-liquefaction strength of the soils around the sliding zone were analyzed. The weak pumice layers crucial to the initiation of the Iburi landslides were further confirmed. In addition, correlation analysis between the Iburi landslide distribution and the pyroclastic fall deposit distribution was performed. The controlling role of the Ta-d pumice on the Iburi landslide occurrence was highlighted. Detailed conclusions of this work are summarized as follows:

1. All the 5625 coseismic landslides, except for 2 deep-seated landslides, are shallow debris slides. The majority of the shallow debris slides initiate due to the localized liquefaction of the weak sliding zone at Ta-d pumice. Three types of downslope movements—steep translational sliding, gentle translational sliding, and the mobilization of V-shaped convergent sliding masses—are generated controlled by the geomorphology.
2. The medium sandy Ta-d pumice MS and the fragile Ta-d pumice CS show lower anti-liquefaction strength than the paleosol and Ta-d pumice FG. Localized liquefaction initially occurs in Ta-d pumice MS or CS layers under intense ground motion. The liquefied zone further develops to the overall displacement of the pyroclastic fall deposits mantled on the liquefied zone.
3. The stable low-permeability paleosol layer underlying the Ta-d pumice enables the seepage flow parallel to the slope and further results in the erosion and weathering of the Ta-d pumice. This explains the extensive existence of the Ta-d pumice MS or fragile Ta-d pumice CS in the landslide distribution area.
4. Statistical analysis indicates that the occurrence and distribution of the coseismic landslide are highly consistent with the distribution of the Ta-d pumice.
5. The area mantled with the weak Ta-d pumice is likely to suffer from massive slope failures when the PGA is larger than 5 m/s^2. This study can provide a guideline for future disaster mitigation operations for this area and a reference for similar areas covered by strong-weathered pumice.>

Acknowledgments

The authors want to thank Tetsuya INUI for providing useful information in the field investigation and visit to the local geological museum. The authors express their sincere gratitude to Prof. Jingshan Bo, Prof. Ping Li, Dr. Xiaobo Li (Institute of Disaster Prevention, China), Dr. Feng Ji (Chengdu University of Technology, China), Dr. Zili Dai, Prakash Dhungana, Kounghoon Nam, and Akinori Iio (Shimane University, Matsue, Japan) for their kind assistance in the field work. We gratefully acknowledge the support provided by the local government and the local museum. We sincerely appreciate the valuable comments and suggestions from the editor and reviewers which considerably improves this work. Ran Li also acknowledged China Scholarship Council (CSC) for financially supporting the study in Shimane University, Japan.

Funding information

This study was financially supported by the fund "Initiation and motion mechanisms of long runout landslides due to rainfall and earthquake in the falling pyroclastic deposit slope area" (JSPS-B-19H01980, Principal Investigator: Fawu Wang) and Fundamental

Research Grant (2017–2019) of Shimane University on "Development of prediction and mitigation technologies on natural disasters in subduction zone using San-in region as a research field."

References

Faris F, Wang F (2014) Investigation of the initiation mechanism of an earthquake-induced landslide during rainfall: a case study of the Tandikat landslide, West Sumatra, Indonesia. Geoenvironmental Disasters 1(1):4–18. https://doi.org/10.1186/s40677-014-0004-3

Fukuoka M (1966) Damage to civil engineering structures. Soils Found 6(2):45–52. https://doi.org/10.3208/sandf1960.6.2_45

Furukawa R, Nakagawa M (2010) Geological map of Tarumae Volcano 1:30,000. Geological map of volcanoes 15. Geological survey of Japan, AIST

Geospatial Information Authority of Japan, GSI (2018) The 2018 Hokkaido eastern Iburi earthquake: fault model (preliminary). https://www.gsi.go.jp/cais/topic180912-index-e.html. Accessed 12 Oct 2018

Gorum T, van Westen CJ, Korup O, van der Meijde M, Fan X, van der Meer FD (2013) Complex rupture mechanism and topography control symmetry of mass-wasting pattern, 2010 Haiti earthquake. Geomorphology 184:127–138. https://doi.org/10.1016/j.geomorph.2012.11.027

Gratchev I, Towhata I (2010) Geotechnical characteristics of volcanic soil from seismically induced Aratozawa landslide, Japan. Landslides 7(4):503–510. https://doi.org/10.1007/s10346-010-0211-2

Harp EL, Jibson RW, Kayen RE, Keefer DK, Sherrod BL, Carver GA, Collins BD, Moss RE, Sitar N (2003) Landslides and liquefaction triggered by the M 7.9 Denali fault earthquake of 3 November 2002. GSA Today 13(8):4–10. https://doi.org/10.1130/1052-5173(2003)013%3C0004:LALTBT%3E2.0.CO;2

Hirose W, Kawakami G, Kase Y, Ishimaru S, Koshimizu K, Koyasu H, Takahashi R (2018) Preliminary report of slope movements at Atsuma Town and its surrounding areas caused by the 2018 Hokkaido Eastern Iburi Earthquake. Rep Geol Sur Hokkaido 90:33–44

Ishihara K, Okusa S, Oyagi N, Ischuk A (1990) Liquefaction-induced flow slide in the collapsible loess deposit in Soviet Tajik. Soils Found 30(4):73–89. https://doi.org/10.3208/sandf1972.30.4_73

Japan Meteorological Agency (2018a) Technical Description-2 Magnitude Determination. https://www.data.jma.go.jp/svd/eqev/data/nwptac/tech2.html. Accessed 12 Oct 2018

Japan Meteorological Agency (2018b) The 2018 Hokkaido Eastern Iburi Earthquake-Portal-.http://www.jma.go.jp/jma/menu/20180906_iburi_jishin_menu.html. Accessed 12 Oct 2018

Kimura G (1994) The latest cretaceous-early Paleogene rapid growth of accretionary complex and exhumation of high pressure series metamorphic rocks in northwestern Pacific margin. J Geophys Res Solid Earth 99(B11):22147–22164. https://doi.org/10.1029/94JB00959

Li GX (2004) Advanced soil mechanics. Tsinghua Press, Beijing

Liao HW, Lee CT (2000) Landslides triggered by the Chi-Chi earthquake. Proceedings of the 21st Asian conference on remote sensing, Taipei 1-2, pp 383–388

National Research Institute for Earth Science and Disaster Resilience (2019) NIED K-NET, KiK-net, National Research Institute for Earth Science and Disaster Resilience. http://www.kyoshin.bosai.go.jp/kyoshin/quake/index_en.html. Accessed 25 Feb 2019

Ortigao JA (1995) Soil mechanics in the light of critical state theories. Balkema, Rotterdam

Osanai N, Yamada T, Hayashi SI, Kastura SY, Furuichi T, Yanai S, Murakami Y, Miyazaki T, Tanioka Y, Takiguchi S, Miyazaki M (2019) Characteristics of landslides caused by the 2018 Hokkaido eastern Iburi earthquake. Landslides 16(8):1517–1528. https://doi.org/10.1007/s10346-019-01206-7

Ozaki M, Taku K (2014) 1:200,000 land geological map in the Ishikari depression and its surrounding area with explanatory note. Seamless Geoinformation of coastal zone "southern coastal zone of the Ishikari depression", seamless geological map of costal zone S-4, Geological Survey of Japan ALST

Pei X, Zhang X, Guo B, Wang G, Zhang F (2017) Experimental case study of seismically induced loess liquefaction and landslide. Eng Geol 223:23–30. https://doi.org/10.1016/j.enggeo.2017.03.016

Sassa K (1985) The mechanism of debris flows. In: proceedings, 11th international conference on soil mechanics and foundation engineering, San Francisco. 1:1173–1176

Sassa K, Fukuoka H, Scarascia-Mugnozza G, Evans S (1996) Earthquake-induced-landslides: distribution, motion and mechanisms. Soils found. 36(special):53–64. https://doi.org/10.3208/sandf.36.Special_53

Sassa K, Fukuoka H, Wang F, Wang G (2005) Dynamic properties of earthquake-induced large-scale rapid landslides within past landslide masses. Landslides 2(2):125–134. https://doi.org/10.1007/s10346-005-0055-3

Scott RF, Zuckerman KA (1972) Sandblows and liquefaction. The Great Alaska earthquake of 1964-engineering publication 1606. National Academy of Sciences, Washington, D.C, pp 179–189

Seed HB (1968) Landslides during earthquakes due to soil liquefaction. J Geotech Eng Div 194(5):1055–1122

Seed HB, Idriss IM, Makdidi F, Nanerjee N (1975) Representation of irregular stress time histories by equivalent uniform stress series in liquefaction analyses. Report no. UCB/EERC-75/29. Earthquake engineering research Centre, U.C. Berkeley

Shao X, Ma S, Xu C, Zhang P, Wen B, Tian Y, Zhou Q, Cui Y (2019) Planet image-based inventorying and machine learning-based susceptibility mapping for the landslides triggered by the 2018 Mw6.6 Tomakomai, Japan earthquake. Remote Sens 11(8):978. https://doi.org/10.3390/rs11080978

Skempton AW (1954) The pore-pressure coefficients a and B. Geotechnique 4(4):143–147

Tajika J, Ohtsu S, Inui T (2016) Interior structure and sliding process of landslide body composed of stratified pyroclastic fall deposits at the Apporo 1 archaeological site, southeastern margin of the Ishikari lowland, Hokkaido, North Japan. J Geol Soc Jpn 122(1):23–35. https://doi.org/10.5575/geosoc.2015.0037

Takch AE, Sadrekarimi A, Naggar HE (2016) Cyclic resistance and liquefaction behavior of silt and sandy silt soils. Soil Dyn Earthq Eng 83:98–109. https://doi.org/10.1016/j.soildyn.2016.01.004

Tamaki M, Kusumoto S, Itoh Y (2010) Formation and deformation processes of late Paleogene sedimentary basins in southern Central Hokkaido, Japan: paleomagnetic and numerical modeling approach. Island Arc 19(2):243–258. https://doi.org/10.1111/j.1440-1738.2009.00698.x

The Japanese Geotechnical Society (JGS) (2010) Soil test: basic and guidance (the second revision). Maruzen press

Tokimatsu K, Yoshimi Y, Ariizumi K (1990) Evaluation of liquefaction resistance of sand improved by deep vibratory compaction. Soils Found 30(3):153–158. https://doi.org/10.3208/sandf1972.30.3_153

Wang F (1999) An experimental study on grain crushing and excess pore pressure generation during shearing of sandy soils: a key factor for rapid landslide motion. PhD thesis of Kyoto University. Kyoto University Research Information Repository:119

Wang F (2019) Liquefactions caused by structure collapse and grain crushing of soils in rapid and long runout landslides triggered by earthquakes. J Eng Geol 27(1):98–107. https://doi.org/10.13544/j.cnki.jeg.2019-034

Wang WN, Nakamura H, Tsuchiya S, Chen CC (2002) Distributions of landslides triggered by the Chi-chi Earthquake in Central Taiwan on September 21, 1999. Landslides 38(4):318–326. https://doi.org/10.3313/jls1964.38.4_318

Wang F, Wu YH, Yang H, Tanida Y, Kamei A (2015) Preliminary investigation of the 20 August 2014 debris flows triggered by a severe rainstorm in Hiroshima City, Japan. Geoenvisronmental Disasters 2(1):17. https://doi.org/10.1186/s40677-015-0025-6

Wang F, Fan X, Yunus AP, Subramanian SS, Alonso-Rodriguez A, Dai L, Xu Q, Huang R (2019) Coseismic landslides triggered by the 2018 Hokkaido, Japan (Mw 6.6), earthquake: spatial distribution, controlling factors, and possible failure mechanism. Landslides 16(8):1551–1566. https://doi.org/10.1007/s10346-019-01187-7

Wiemer G, Moernaut J, Stark N, Kempf P, De Batist M, Pino M, Urrutia R, de Guevara BL, Strasser M, Kopf A (2015) The role of sediment composition and behavior under dynamic loading conditions on slope failure initiation: a study of a subaqueous landslide in earthquake-prone south-Central Chile. Int J Earth Sci 104(5):1439–1457. https://doi.org/10.1007/s00531-015-1144-8

Xie D (2011) Soil dynamics. Higher Education Press, Beijing

Xu C, Xu X (2014) Statistical analysis of landslides caused by the mw 6.9 Yushu, China, earthquake of April 14, 2010. Nat Hazards 72(2):871–893. https://doi.org/10.1007/s11069-014-1038-2

Xu C, Xu X, Shyu JB (2015) Database and spatial distribution of landslides triggered by the Lushan, China mw 6.6 earthquake of 20 April 2013. Geomorphology 248:77–92. https://doi.org/10.1016/j.geomorph.2015.07.002

Xu L, Coop MR, Zhang M, Wang G (2018) The mechanics of a saturated silty loess and implications for landslides. Eng Geol 236:29–42. https://doi.org/10.1016/j.enggeo.2017.02.021

Yamagata K (1994) Tephrochronological study on the Shikotsu and Kuttara volcanoes in southwestern Hokkaido, Japan. J Geogr 103(3):268–285. https://doi.org/10.5026/jgeography.103.268

Yamagishi H, Yamazaki F (2018) Landslides by the 2018 Hokkaido Iburi-Tobu earthquake on September 6. Landslides 15:2521–2524. https://doi.org/10.1007/s10346-018-1092-z

Yang H, Wang F, Vilimek V, Araiba K, Asano S (2015a) Investigation of rainfall-induced shallow landslides on the northeastern rim of Aso caldera, Japan, in July 2012. Geoenvironmental Disasters 2(1):20–14. https://doi.org/10.1186/s40677-015-0028-3

Yang H, Wang F, Miyajima M (2015b) Investigation of shallow landslides triggered by heavy rainfall during typhoon Wipha (2013), Izu Oshima Island, Japan. Geoenvironmental Disasters 2(1):15–10. https://doi.org/10.1186/s40677-015-0023-8

Zhang S, Wang F (2019) Three-dimensional seismic slope stability assessment with the application of Scoops3D and GIS: a case study in Atsuma, Hokkaido. Geoenvironmental Disasters 6(1):9–14. https://doi.org/10.1186/s40677-019-0125-9

Zhang S, Li R, Wang F, Iio A (2019) Characteristics of landslides triggered by the 2018 Hokkaido Eastern Iburi earthquake, Northern Japan. Landslides 16(9):1691–1708. https://doi.org/10.1007/s10346-019-01207-6

Zlender B, Lenart S (2005) Cyclic liquefaction potential of lacustrine carbonate from Julian Alps. Acta GeotechSlov 1(2):22–31

R. Li · F. Wang (✉) · S. Zhang
Department of Earth Science,
Shimane University,
1060 Nishikawatsu-cho, Matsue, Shimane 690-8504, Japan
Email: wangfw@riko.shimane-u.ac.jp